



Plane-symmetric co-flow capillary for the generation of monodisperse droplets

Yao Gong^{1,2,3} · Lili Zou^{1,2,3} · Jang Min Park⁴ · Kai You^{1,2,3} · Xiang Yi^{1,2,3} · Bin Li⁵

Received: 21 August 2023 / Accepted: 29 November 2023 / Published online: 29 December 2023
© The Author(s), under exclusive licence to Springer-Verlag GmbH Germany, part of Springer Nature 2023

Abstract

This study proposes a novel co-flow capillary microfluidic device that can generate highly monodisperse droplets and polymeric microspheres. The device mainly consists of two self-aligning special-shaped polymeric capillaries. The outer capillary features a gradually contracting and expanding geometry, and the inner has an elliptical cross section at the end. The elliptical nozzle of the inner capillary fits into the contraction region of the outer capillary, and so assembled device, namely a plane-symmetric co-flow capillary, benefits from the self-alignment of the capillaries. The design and manufacturing process of the device are outlined, including a discussion on how the processing conditions affect the capillary geometry. Subsequently, the proposed device is used for droplet generation tests, and the diameter distribution of generated droplets and their influencing factors are investigated. The droplet generation mechanism with the elliptical nozzle is discussed with the help of modeling and simulation. Furthermore, monodisperse porous polymeric microspheres are fabricated using the proposed device, and their porous features are characterized. The results show that the proposed device can produce monodisperse droplets with a mean diameter of a few hundred micrometers and a coefficient of variance (CV) of less than 1%, reflecting the stability of the device. Additionally, porous polymeric microspheres could be successfully produced, and the CV of the size distribution is only around 1%.

Keywords Droplet generation · Capillary-based microfluidics · Plane-symmetric · Co-flow

1 Introduction

Droplet microfluidics has become an essential tool in many application fields, such as in vitro diagnosis, drug delivery, cell biology, and regenerative medicine. This is primarily due to its unique advantages, encompassing high throughput, fast reaction, efficient manipulation of individual fluids, and low reagents consumption (Shang et al. 2017; Zhu and Wang 2017; Hettiarachchi et al. 2021; Trossbach et al. 2022; Du et al. 2023). For practical and commercial applications of droplet microfluidics, the droplet generation process should be stable and controllable to ensure the uniformity of the droplet size (Nguyen et al. 2019; Nie et al. 2019; Li et al. 2020).

There are two types of droplet generation methods: active and passive methods (Zhu and Wang 2017; Montanero and Gañán-Calvo 2020). Active methods use external forces, such as magnetic, electric, acoustic, and laser fields, to perturb the flow and fluid–fluid interface (Zhu et al. 2016; Shams Khorrani and Rezai 2018; Teo et al. 2020; Yin et al. 2020; Bajgiran et al. 2021). In contrast, passive methods are

✉ Lili Zou
lilizou@mail.ustc.edu.cn

✉ Jang Min Park
jpark@yu.ac.kr

¹ Institute of Biological and Medical Engineering, Guangdong Academy of Sciences and National Engineering Research Center for Healthcare Devices, Guangzhou 510500, Guangdong, China

² Guangdong Engineering Technology Research Center for Diagnosis and Rehabilitation of Dementia, Guangzhou 510500, China

³ Guangdong Key Lab of Medical Electronic Instruments and Polymer Material Products, Guangzhou 510632, People's Republic of China

⁴ School of Mechanical Engineering, Yeungnam University, Gyeongsan 38541, Republic of Korea

⁵ School of Intelligent Manufacturing, Sichuan University of Arts and Science, Dazhou 635000, Sichuan, China

more attractive for researchers because of their convenience, utilizing the microchannel geometry to manipulate the flow. In these cases, viscous stress can break off a droplet, or interface instability can lead to a break-up of a jet into multiple droplets (Deng et al. 2017; Hoang et al. 2018; Langer et al. 2018; Yao et al. 2019; Ibrahim et al. 2021). Therefore, the core of the passive approach lies in the construction strategy of the microchannel, encompassing geometry design and fabrication techniques.

Representative microchannels employed in passive methods include cross-flow, flow focusing, and co-flow geometries (Glawdel et al. 2012; Wang 2015; Mottaghi et al. 2020). Cross-flow geometries, such as a T- or Y-junction, are commonly fabricated using lithography in laboratories, and, therefore, the microchannel has a quasi-two-dimensional geometry (Shui et al. 2008; Abate and Weitz 2011). Similarly, co-flow and flow-focusing geometries also can be constructed into quasi-2D planar microchannels (Hettiarachchi et al. 2021; Ibrahim et al. 2021). However, three-dimensional axisymmetric microchannels are often preferred due to the advantages in droplet generation and protection against adhesion at the wall, reliability of the microfluidic device under high flow rate conditions, and potential for commercial applications (Takeuchi et al. 2005; Deng et al. 2017; Zhang et al. 2019; Montanero and Gañán-Calvo 2020). The 3D coaxial microfluidic devices can be realized by assembling capillaries (glass or polymer) (Utada et al. 2007; Zhu et al. 2015; Deng et al. 2017; Zhou et al. 2017), molding PDMS over a fiber (Takeuchi et al. 2005), and 3D printing (Nguyen et al. 2019; Dewandre et al. 2020; Gyimah et al. 2021). In general, PDMS molding requires high costs, and 3D printing is limited by production efficiency and resolution (Zhu and Wang 2017). In contrast, capillaries are commercially available standard components, making them highly promising for practical applications. However, ensuring concentricity between the capillaries is critical.

In coaxial capillary microchannels, it is crucial for the inner capillary to be precisely centered along the axis of the outer capillary. In view of the device fabrication, aligning two capillaries demands careful attention (Zhu and Wang 2017). The earlier and most widely accepted way for the alignment is to use a circular tube whose outer diameter matches the inner dimension of a square tube (Utada et al. 2007; Zhu et al. 2015; Deng et al. 2017; Zhou et al. 2017). Also, recent advancements in 3D printing enables precise assembly of nozzles and capillaries (Dewandre et al. 2020). To our knowledge, however, these existing methods heavily rely on cutting-edge manufacturing techniques, and, therefore, the cost is relatively high. As a consequence, not much attention has been paid to the alignment method based on mature manufacturing techniques, presumably because the primary interest lies in the droplet generation rather than the details of the device fabrication.

This study proposes a novel plane-symmetric co-flow device for generating monodisperse droplets. This is achieved using specially shaped capillaries, which are fabricated using hot stretching and cutting processes, facilitating self-alignment, flexible control, and efficient manufacturing of the device. The design and fabrication process of the proposed device will be described first. Subsequently, the device's performance in droplet generation will be evaluated. The droplet generation mechanism will be also discussed with the help of modeling and simulation. The effect of flow condition and capillary geometry on the droplet size will be discussed. Furthermore, it will be demonstrated that monodisperse porous polymer microspheres can be fabricated using the proposed device. Finally, a short summary and discussion conclude the study.

2 Plane-symmetric co-flow microchannel

2.1 Design

Figure 1a shows schematic diagrams describing the proposed co-flow microchannel. It consists of two distinct special-shaped polymeric capillaries: the outer capillary is an axisymmetric contraction–expansion capillary; the inner one has an elliptical cross-section (elliptical nozzle) at the end. The two capillaries are assembled such that the major axis of the elliptical nozzle of the inner capillary is fitted to the inner wall of the outer capillary. This precise alignment mechanism fosters self-alignment. Consequently, this arrangement yields a three-dimensional plane-symmetric co-flow microchannel. In contrast to the previous co-flow devices shown in Fig. 1b (Utada et al. 2007; Zhu and Wang 2017), the proposed one has the inner nozzle mechanically secured by the outer capillary. This mechanical fixation and the self-alignment with the elliptical nozzle are the distinguishing features of the proposed co-flow microchannel.

2.2 Fabrication

Figure 2 shows the fabrication method of the outer capillary alongside an example of the outcome. The contraction–expansion geometry of the outer capillary could be achieved through, namely, a hot stretching process. A uniform capillary is locally heated to a specific temperature. Then, the capillary is uniaxially stretched at a constant rate. The stretched capillary is then air-cooled at room temperature. In this study, a commercial polytetrafluoroethylene (PTFE) capillary (Hongfu Insulation Material Co., LTD, Dongguan, China) is used for the outer capillary, and it has outer and inner diameters of 0.8 and 0.3 mm, respectively.

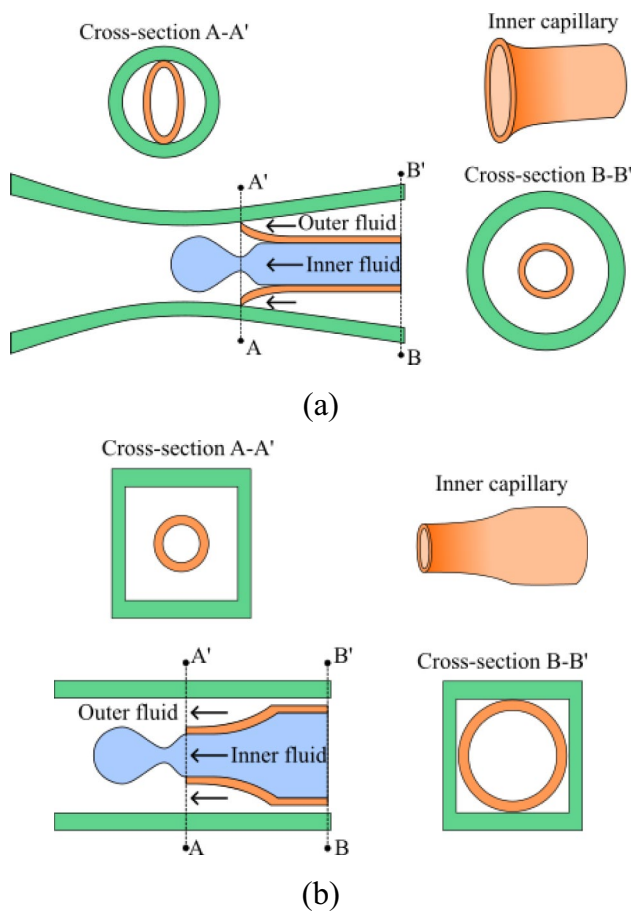
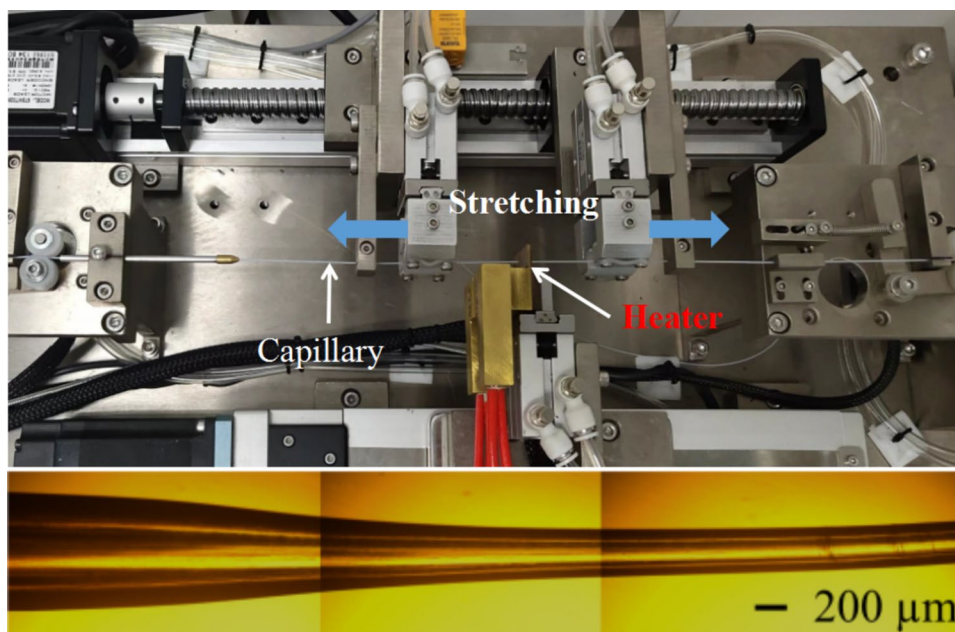


Fig. 1 Schematic diagrams of **a** the proposed plane-symmetric co-flow microchannel and **b** a previous co-flow microchannel (Utada et al. 2007a, Zhu and Wang 2017)

Fig. 2 A schematic diagram of the hot stretching process and a microscopic image of the hot stretched capillary with $T_s = 370\text{ }^\circ\text{C}$ and $E = 10$



The heating temperature (T_s) and elongation are the two major parameters of the hot stretching process. The elongation (E) is defined as follows:

$$E = \frac{l - l_0}{l_0}, \tag{1}$$

where l_0 and l are the initial and final lengths of the stretched region, respectively. Since the stretching takes place mostly at the heated region, the initial length, l_0 , is assumed to be the length of the heater, while the stretching length, $l - l_0$, is a processing parameter. The microscopic image shown in Fig. 2 corresponds to the result of $T_s = 370\text{ }^\circ\text{C}$ and $E = 10$.

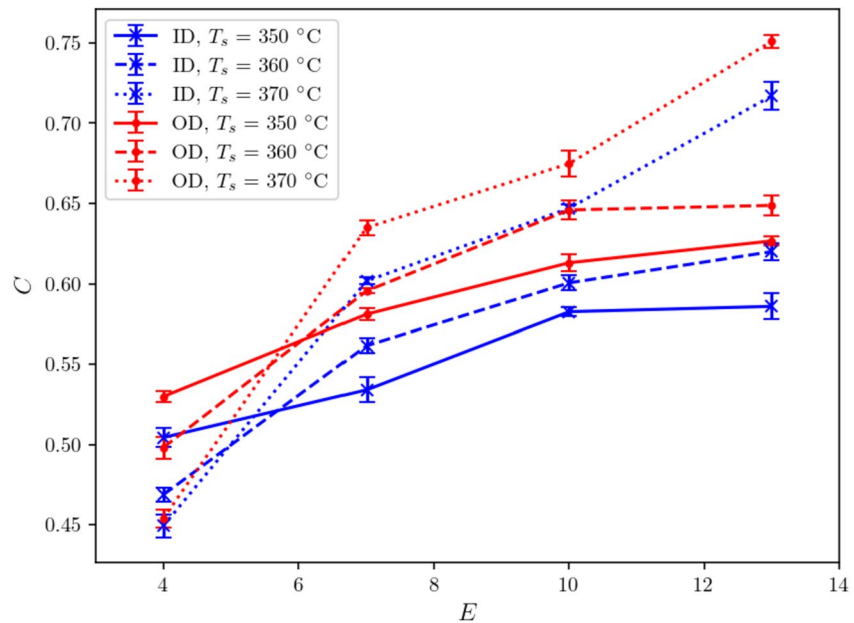
To attain the desirable co-flow geometry as described in Fig. 1a, the contraction diameter of the outer capillary should be small enough to match the elliptical nozzle of the inner capillary. In this regard, several experiments are carried out to characterize the effect of the processing condition on the contraction ratio of the stretched capillary. The contraction ratio (C) is defined as follows:

$$C = \frac{D_0 - D}{D_0}, \tag{2}$$

where D_0 is the diameter before the stretching, and D is the minimum diameter at the contraction of the stretched capillary.

The effect of the heating temperature and the elongation on the contraction ratio is shown in Fig. 3. Four samples were fabricated for each condition, and the average value and the standard deviation of the contraction ratio are shown. The contraction ratio increases with the elongation in general. The outer diameter shows a larger contraction ratio than the inner one due to the reduction in capillary wall thickness

Fig. 3 Relationship between elongation and contraction ratio of the hot stretched PTFE capillary at various heating temperatures



during the hot stretching process. Moreover, it could also be found that the temperature plays an important role in the stretching of the capillary. The contraction ratio tends to increase with the heating temperature.

A significant stretching can result in damage to the capillary, for example, in the case of $T_s = 370$ °C and $E = 13$ in Fig. 3. In this study, we use the capillary stretched at $T_s = 370$ °C and $E = 10$ which results in the inner contraction ratio of 0.649 corresponding to the inner diameter of 0.105 mm (a microscopic image shown in Fig. 2). This contraction ratio allows best fit with the elliptical nozzle of the inner capillary of which fabrication is explained below.

The elliptical cross section at the end of the inner capillary can be achieved by employing V-shaped cutters, as shown in Fig. 4. A polyether-ether-ketone (PEEK) capillary (Yijia Technology Co., LTD, Beijing, China) is used, which has outer and inner diameters of 0.1 mm and 0.05 mm, respectively. After cutting the inner capillary with V-shaped cutters at room temperature, a heat treatment process is followed. This process serves to relax

residual stress which develops during the cutting process. During the heat treatment process, the deformation will partially recover due to the viscoelastic nature of the polymer, and the final shape of the cross-section depends on the heat treatment condition.

In this study, several experiments are carried out with different heat treatment temperatures ranging from 140 °C to 180 °C, while the heat treatment time is fixed at 10 min. Figure 5 shows the effect of the heat treatment temperature on the final shape of the elliptical cross-section. For each condition, four samples were fabricated. The geometric parameters, denoted as a_1 , a_2 , b_1 , and b_2 in Fig. 4, are measured. It might be mentioned that parameter a_1 is relevant for the assembly with the outer capillary (see Fig. 1), while parameters a_2 and b_2 will affect the pinch-off process during the droplet generation. The elliptical shape depends on the heat treatment temperature at $T < 160$ °C, but it is almost constant at $T \geq 160$ °C suggesting enough relaxation of the residual stress. Unless otherwise mentioned, we use the inner capillary treated at 160 °C which results

Fig. 4 Schematic diagram of the cutting process and a microscopic image of the cross-section of the cut

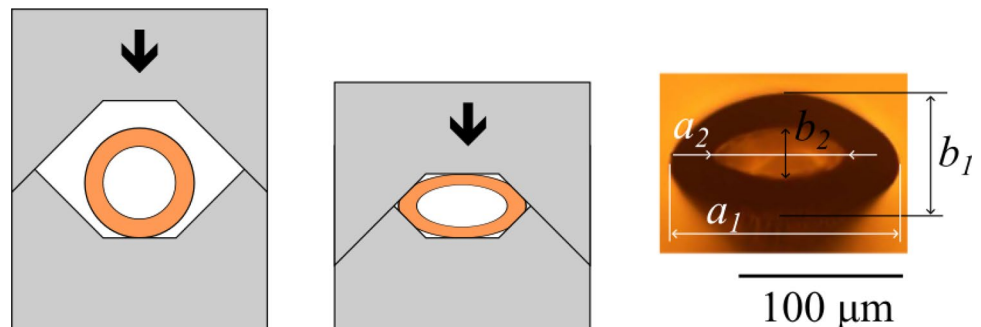


Fig. 5 Dimensions of the elliptical nozzle of the inner capillary for different heat treatment temperatures

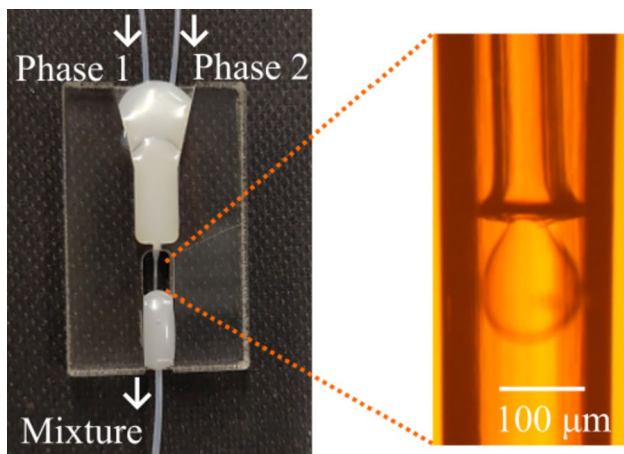
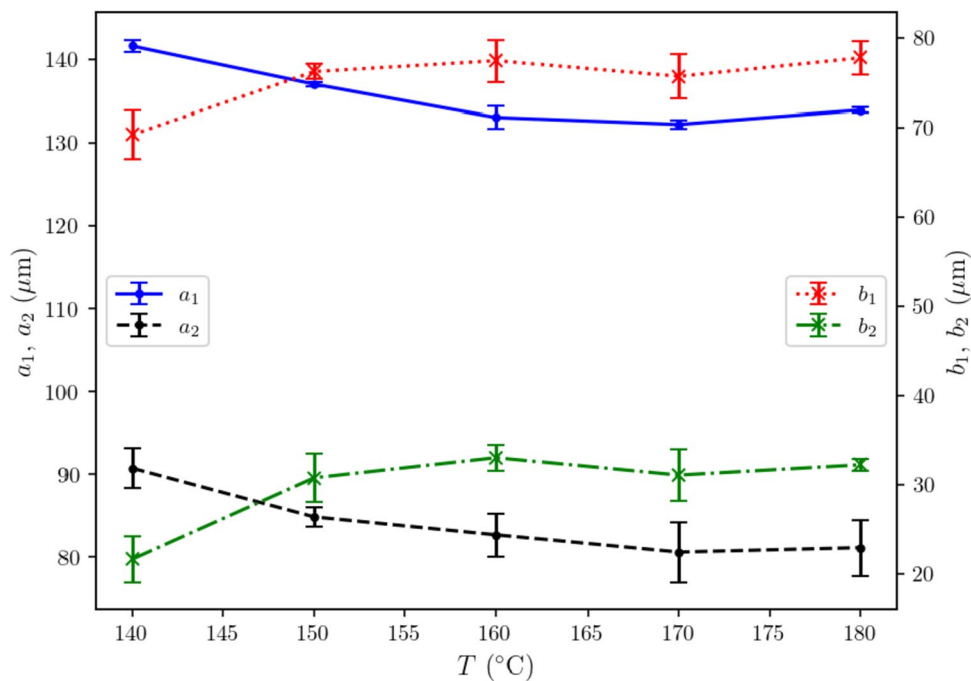


Fig. 6 A picture of the droplet generation chip and a microscopic image (top view) of the plane-symmetry co-flow microchannel

in $a_1=133 \mu\text{m}$, $a_2=83 \mu\text{m}$, $b_1=77 \mu\text{m}$, and $b_2=33 \mu\text{m}$ (a microscopic image shown in Fig. 4).

The inner capillary is inserted into the outer one until the elliptical nozzle is fitted to the contraction capillary, as shown in Fig. 6. These capillaries are then connected with two additional unprocessed PTFE capillaries that, respectively, deliver the oil and water phases. The assembled plane-symmetric co-flow microchannel is affixed onto a polymethyl methacrylate (PMMA) substrate using a hot melt adhesive, and the droplet generation chip is finally completed as shown in Fig. 6.

3 Droplet generation

3.1 Experimental

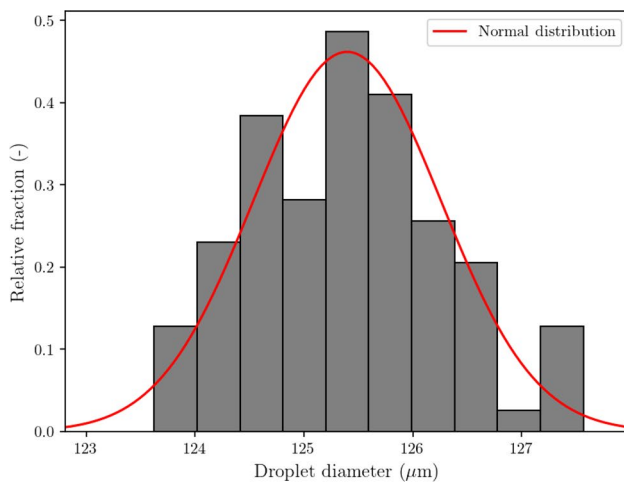
Deionized water and fluorinated oil (dSURF, Fluigent) are supplied to the inner and outer capillaries, respectively. Surfactant (perfluorocarbon–PEG copolymer) is used to stabilize droplets. The outlet is connected to a collecting container. A CCD microscope camera (CM2000, Runzebaifu Tech. Co., Ltd. China) is used to observe the droplet generation process and measure the diameter (d) of the generated droplet. Eight samples are collected for each experiment. The collected droplets are spread onto a concave glass slide for precision measurement.

We use two different ways to drive the flow. The first approach is applying negative pressure to the collecting container using a diaphragm pump (D30GE-4521-24V-BLDC, WE PUMP Co. LTD, Shenzhen, China). The pressure ranges from -5 to -40 kPa. This approach benefits from the simplicity of the equipment, enabling a continuous production of the droplets, but the flow rates of each phase cannot be explicitly controlled. The second method is to use syringe pumps (Model NE-1000, New Era Pump Systems, Inc., New York, USA) connected to each inlet capillary. This approach allows precise control of the flow rates of each phase, but the droplet generation process is limited by the size of the syringes used. The flow rate of the water phase (Q_{in}) is held constant at $0.5 \mu\text{L}/\text{min}$ or $0.2 \mu\text{L}/\text{min}$, while the flow rate ratio ($\frac{Q_{out}}{Q_{in}}$ where Q_{out} is the flow rate of the oil phase) varies between 1, 2, 3, and 4.

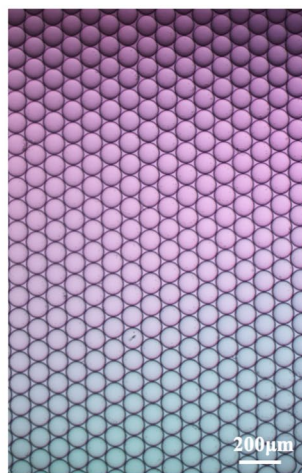
3.2 Pressure-driven droplet generation

Figure 7 shows the generated droplets and their size distribution when negative pressure of -15 kPa is applied to the collecting container. The diameter of the droplets is $125.40 \pm 0.86 \mu\text{m}$ ($\text{CV} = 0.689\%$; $\text{PDI} = 1.00015$). This result underscores the stability of the present plane-symmetry co-flow microchannel, attributed to the mechanical fit of the nozzle. It might be noted that recent co-flow devices have achieved a CV of approximate 2–3% (Zhu et al. 2016; Zhang et al. 2021), highlighting the performance of the proposed device.

Figure 8 shows the effect of driving pressure on droplet diameter for different cases of the elliptical nozzle. Three different elliptical nozzles (E1, E2 and E3 shown in Fig. 9) are used, and their dimensions are summarized in Table 1. With



(a)



(b)

Fig. 7 **a** Diameter distribution of droplets generated by the plane-symmetric co-flow microchannel and **b** a microscopic image of the droplets

the nozzles E1 and E2, the droplet size decreases with increasing the driving pressure from 5 to 30 kPa, which is a typical characteristic of the dripping regime (Fu et al. 2012; Deng et al. 2017). As the pressure is increased further, the droplet size begins to increase slightly, indicating the onset of the jetting regime (Utada et al. 2007; Zhu et al. 2016). However, with the thinnest nozzle E3, the droplet size does not follow the above dependency to the driving pressure. Interestingly, the droplet diameter increases and then decreases with the applied pressure. This result suggests that the droplet generation mechanism with a thin nozzle is different from that of conventional co-flow geometry.

It should be mentioned that the previous study using thin expanding nozzles noted that the droplet size is independent of the flow rate (Amstad et al. 2016). With the help of the numerical simulation, they could find that the droplet generation is driven by the instability of the interface, and, therefore, the droplet size depends only on the nozzle geometry.

The diameter of the droplets generated with the thin nozzle E3 at lower pressure (shown in Fig. 8) is $101 \mu\text{m}$, and its ratio to the minor axis (b_2) of the elliptical nozzle is 4.81. This ratio is close to 4.51 above which the instability develops (Rayleigh 1878). Therefore, the result suggests that the instability characterizes the droplet size in this regime. As the pressure increases, however, the droplet diameter increases. This transition is likely to be due to the interplay between the instability, interfacial tension, viscous force and inertia effect. At higher pressure, the droplet size decreases with the pressure, similar to the other cases with E1 and E2.

It is worth noting that across all considered cases, the CV values of the droplet size remain below 1%. Table 2 compares the result with other recently developed co-flow devices.

3.3 Modeling and simulation

In the dripping regime, the droplet size can be estimated using a simple model which considers the balance between interfacial tension and viscous drag force (Umbanhowar et al. 2000). The balance equation reads

$$h\gamma = 3\pi\eta(d - D_n)(v - v_d), \quad (3)$$

where h is the perimeter of the nozzle, γ is the interfacial tension, η is the viscosity, d is the droplet diameter, D_n is the diameter of the nozzle, v is the mean velocity of the outer phase, and v_d is the droplet velocity. The right-hand side of the equation represents the drag force approximated by Stokes law. Particularly in this study, the nozzle has elliptical cross section, and, therefore, it is unclear how to define the diameter D_n . One might introduce hydraulic diameter, but we found that the experimental result can be better fit using the length of major axis, $2a_2$.

Fig. 8 Effect of the driving pressure and nozzle shape on the generated droplet size

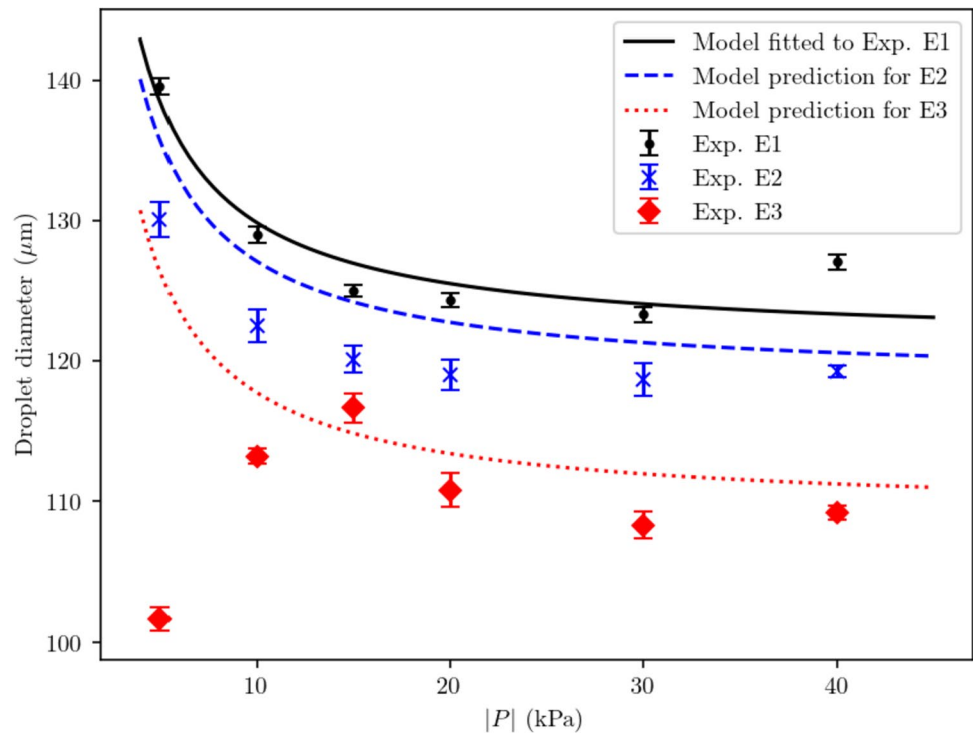


Fig. 9 Microscopic images of the elliptical nozzles

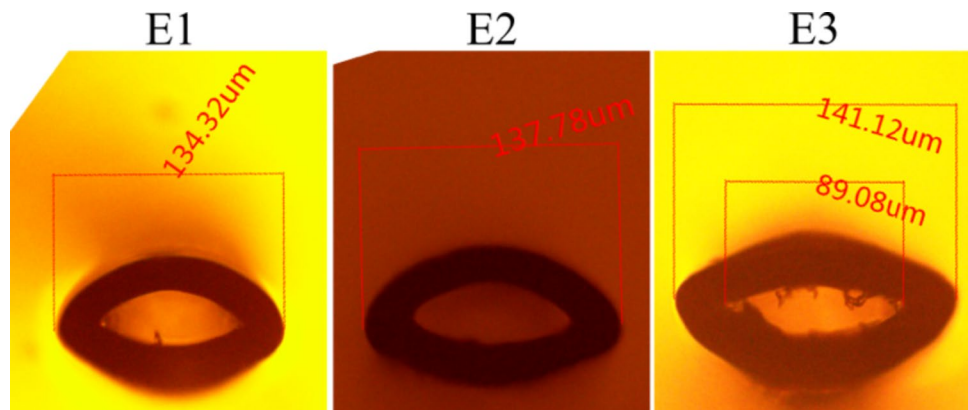


Table 1 Dimensions and areas of the elliptical nozzles

Nozzle	a_2 (µm)	b_2 (µm)	Area (µm ²)
E1	81	33	8397.5
E2	84	30	7916.8
E2a	85.7	27	7272.9
E2b	87.9	24	6631.4
E3	89	21	5871.6

Table 2 Recently developed co-flow capillary microchannels and the size of droplets generated in dripping regime

Reference	Droplet diameter (µm)	CV (%)	Note
Zhu et al. (2016)	~ 100	2	Vibration-induced fluctuation
Zhang et al. (2021)	200–500	3	3D printed device
Present study	100–140	1	Elliptical nozzle

Assuming that $v_d \ll v$, one can arrive at the following simple model (Umbanhowar et al. 2000):

$$d = 2a_2 + \frac{h\gamma}{3\pi\eta v}. \quad (4)$$

The outer phase velocity can be written as $v = \frac{Q_{out}}{A_{out}}$, where Q_{out} is the outer phase volumetric flow rate and A_{out} is the cross-sectional area of the outer capillary channel. Assuming the flow is fully developed laminar, one may introduce the Poiseuille law, $Q_{out} \sim |P|$. After introducing some fitting parameters, the model is rewritten as follows:

$$d = \alpha a_2 + \frac{\beta}{|P|}, \quad (5)$$

where α and β are the fitting parameters. The model is fitted to the experimental data for nozzle E1 (Fig. 8), and the fitted parameters are $\alpha = 1.347$ and $\beta = 86.71$ kPam, respectively. The model predictions for the other nozzles of E2 and E3 are shown in Fig. 8. The model agrees with the experimental data for the case with nozzle E2.

However, the experimental result with nozzle E3 shows some discrepancy with the model prediction, especially at lower pressure condition. The droplet size is much smaller than the prediction by the model. As discussed before, this suggests that the droplet generation mechanism with the elliptical nozzle can be different from that of the conventional co-flow devices.

To better understand the effect of nozzle shape on the droplet diameter, numerical simulation is carried out using the Surface Evolver (Brakke 1992). This simulation solves the equilibrium state of the interface by minimizing the total energy of the system under a given condition, and it does not take the hydrodynamic effect into account. In this study, we examine if the nozzle shape can affect the equilibrium shape of the droplet, assuming a quasi-static state. Five different nozzles are considered as shown in Table 1, where nozzles E2a and E2b are added to better represent the result, and their dimensions are determined by linear interpolation between the dimensions of E2 and E3.

Details of the numerical procedure is similar to the previous work (Rayner et al. 2004), but one more constraint is imposed to consider the confinement effect due to the presence of outer capillary. The droplet is always in contact with the elliptical edge of which dimension is shown in Table 1, and the contact angle of 90 degree is applied. The interfacial tension of 0.01 N/m is applied. The diameter of the outer capillary is 130 μm . The Surface Evolver successively solves the equilibrium state while the droplet volume is increased. The stability of the droplet is examined at each incremental step using eigenvector analysis, from which we can find the maximum stable volume of the droplet.

Figure 10 shows the simulation result, and the droplet size generally decreases as the nozzle becomes thinner. The

droplet diameter is limited up to 130 μm which is because of the constraint due to the outer capillary. For the thin nozzle E3, the droplet diameter is 72 μm which is smaller than the experimental data of 101 μm in Fig. 8. Considering that the force balance model of Eq. (3) predicts much larger droplet size than the experimental result, the simulation result suggests that the droplet generation mechanism with the thin nozzle involves instability of the interface, as discussed above. In other words, with the thin nozzle E3, the decrease of the droplet size as the pressure is decreased as shown in Fig. 8 could be due to the instability of the interface.

3.4 Effect of the flow rate

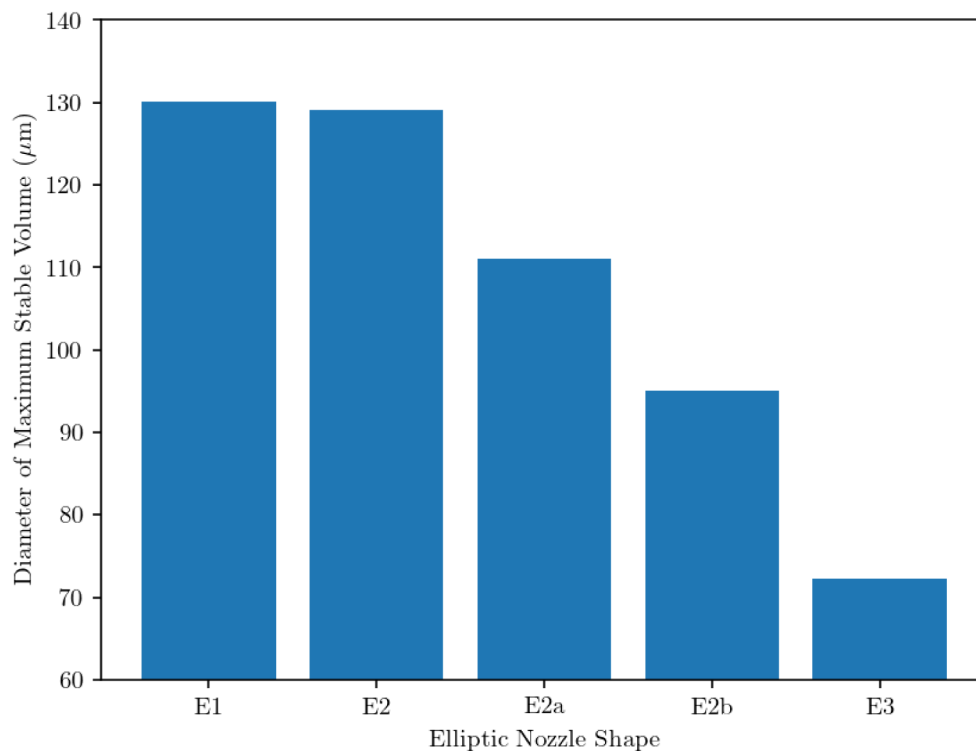
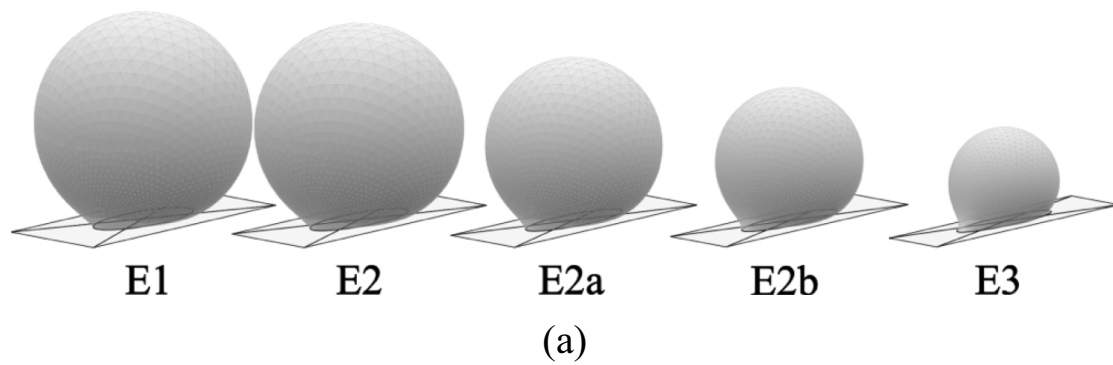
Two syringe pumps are used for precise control of the flow rates of each phase. Figure 11 shows the microscopic images of the droplet generation under different flow rate conditions (see also the supplementary videos). In this dripping regime, the droplet size decreases as the relative velocity of the outer phase increases. This is because the increased outer phase could drag the inner phase into a thinner stream. Similarly, the droplet size decreases as the total flow rate increases while the flow rate ratio is fixed, as can be explained by the balance between the interfacial tension and viscous drag force (Tan et al. 2004; Utada et al. 2007). The average droplet diameters for different flow rate conditions are summarized in Fig. 12. Within the considered range of flow rates, the droplet size could be precisely controlled, spanning from 100 to 500 μm .

3.5 Synthesis of porous microspheres

Porous gel microspheres with three-dimensional structures provide effective environment for cell growth and proliferation, and thus their fabrication has been of practical interest in the field of 3D cell culture (Huang et al. 2018). Compared to the emulsification method, the microfluidic approach can offer an advantage regarding the uniformity of the microspheres (Amoyav and Benny 2019). Leveraging the present plane-symmetric co-flow device, porous polymer microspheres are manufactured in this study.

Paraffin oil containing 10% of surfactant (Span-80) is used as the continuous outer phase. The inner phase is prepared by dissolving 1 g of methacrylate gelatin in 10 mL of phosphate-buffered saline (PBS) solution containing 0.25% (w/v) of the lithium phenyl-2,4,6-trimethylbenzoylphosphinate (LAP) photoinitiator at 40 $^{\circ}\text{C}$. A vacuum pressure of -5 kPa is applied and the generated droplets are exposed to UV light of a wavelength of 405 nm for 30 s to crosslink and solidify the methacrylate gelatin. The microspheres are collected and then eluted with n-hexadecane, surfactant, and deionized water to obtain purified polymer microspheres.

The microscopic image of the UV-crosslinked gel particles is shown in Fig. 13. The mean diameter of microspheres



(b)

Fig. 10 Surface Evolver simulation results for different nozzle shapes: **a** droplet shapes of the maximum stable volume and **b** their diameter

is $211 \pm 2.82 \mu\text{m}$ ($\text{CV} = 1.33\%$; $\text{PDI} = 1.00053$). The lyophilized microspheres are observed under a scanning electron microscope (SEM, PhenomWorld Co., Ltd., China), and it is found that the microsphere has a porous structure accompanied by a certain degree of shrinkage deformation. The mean diameter of the lyophilized porous polymer microspheres is $150 \pm 5 \mu\text{m}$ ($\text{CV} = 3.33\%$; $\text{PDI} = 1.0033$), and the pore size is about 20 to 40 μm , which is enough to hold a stem cell. The porous structure of the microcarrier may regulate cell attachment, proliferation, migration, and cell–cell interactions, and

provide larger spaces for nutrients, oxygen, and waste product diffusion.

4 Conclusions

A novel plane-symmetric co-flow capillary device is proposed, and its performance of generating highly monodisperse droplets is investigated. The out and inner capillaries could be fabricated by hot stretching and V-cutting

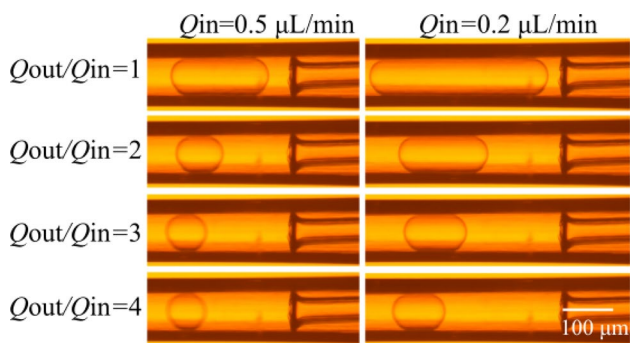


Fig. 11 Microscopic images of the droplet generation for different flow rate conditions (see also the supplementary videos). Q_{out} and Q_{in} are, respectively, the outer (oil) phase and inner (water) phase flow rates

processes, respectively. The dimensions of the contraction–expansion microchannel and elliptical nozzle could be tailored by varying the processing parameters so that the two capillaries can be assembled simply by inserting the inner capillary into the outer one. Especially the elliptical nozzle of the inner capillary assists the self-alignment at the center of the outer capillary, which enables simple assembly of the capillaries.

The proposed microfluidic device could generate highly monodisperse droplets with a coefficient of variance of less than 1%, reflecting the stability of the device. We could control the mean diameter of the droplets from 100 to 500 μm while the small CV value is maintained. As an

Fig. 12 Effect of flow rates on the droplet size. Q_{out} and Q_{in} are, respectively, the outer (oil) phase and inner (water) phase flow rates

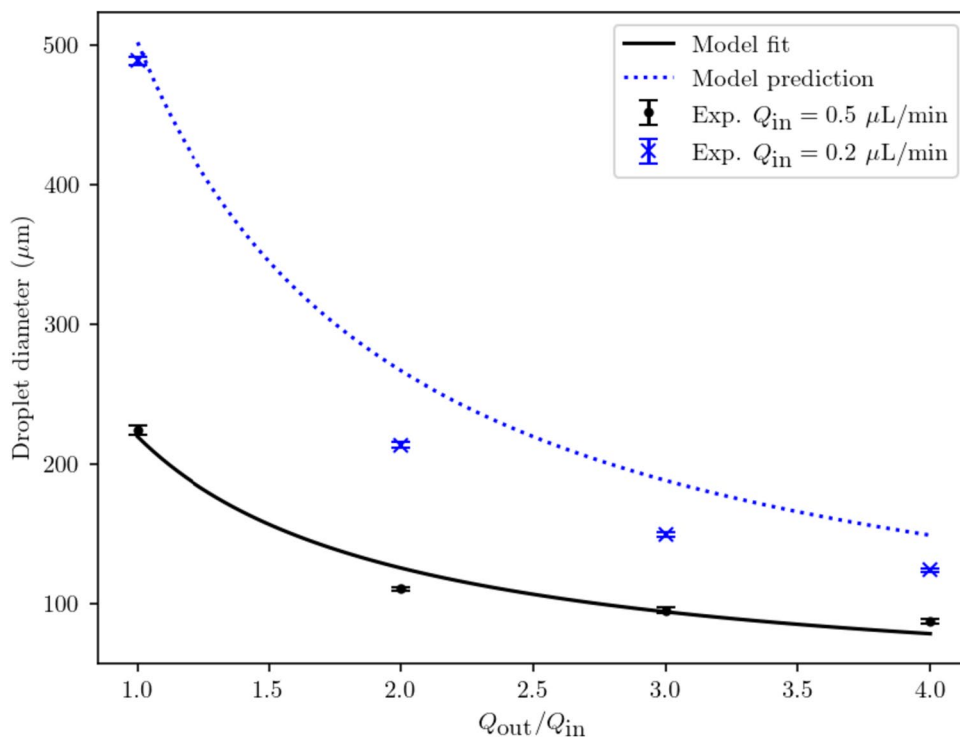
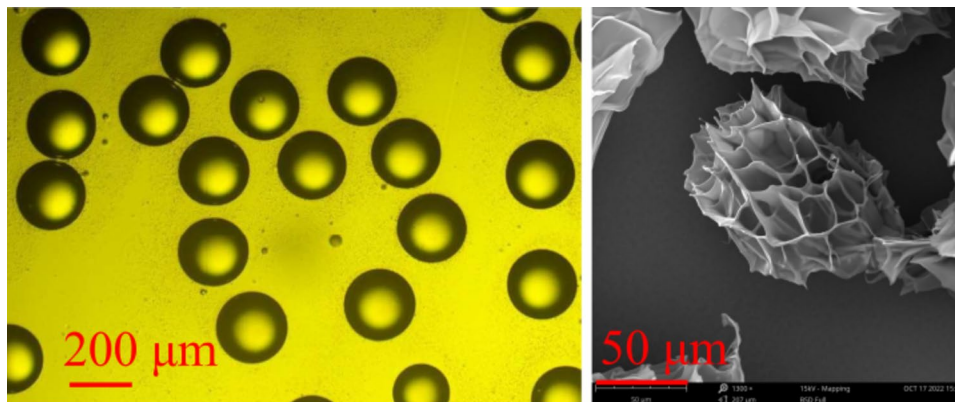


Fig. 13 Microscopic image of the polymer droplets (left) and SEM image of the porous microspheres after solidification (right)



example of the practical application of the device, we successfully produced porous polymer microspheres.

Especially, it was found that the droplet generation mechanism with the elliptical nozzle can be different from the conventional co-flow geometry with a circular nozzle. The experimental result for lower driving pressure condition suggested that the droplet size is affected by the instability of the interface when the nozzle has a thin cross-section. To examine the effect of nozzle cross-sectional shape on the droplet size, numerical simulation was carried out using the Surface Evolver. The droplet size generally decreased as the nozzle becomes thinner, suggesting that the decrease of the droplet size as the nozzle becomes thinner could be due to the instability of the interface.

The proposed device consists of polymeric capillaries and adhesives, and, therefore, it can be easily manufactured at a low cost while it is shown to be robust and stable enough without suffering from failure or leakage issues during droplet generation. In addition, the present device allows a larger gap between the two capillaries, so we expect that the flow resistance and hydraulic pressure in the outer stream can be much reduced compared to the conventional co-flow capillary where the outer diameter of the inner capillary must match the inner dimension of the outer square tube. Extending the current device to a parallel system with multiple capillaries would be straightforward.

Supplementary Information The online version contains supplementary material available at <https://doi.org/10.1007/s10404-023-02703-x>.

Acknowledgements We express our gratitude to the reviewers for the insightful comments, which greatly contributed to the enhancement of the paper.

Author contributions Y.G.: investigation, methodology, formal analysis, manuscript writing, and supervision; L.Z.: funding acquisition, formal analysis, manuscript review and editing; J.M.P.: formal analysis, modeling and simulation; manuscript review and editing; K.Y.: investigation; X.Y.: investigation; B.L.: manuscript modification and validation.

Funding This work was supported by GDAS' Project of Science and Technology Development (grant numbers 2021GDASYL-20210103029, 2021GDASYL-20210103027, 2022GDASZH-2022020402-01, 2022GDASZH-2022010110, 2021GDASYL-20210302002); Innovation Foundation Project of Institute of Biological and Medical Engineering, Guangdong Academy of Sciences (0523185001) and Science and Technology Program of Guangzhou (202102021028); Natural Science Foundation of Sichuan Province (NO.22NSFSC1989); Basic Science Research Program through the National Research Foundation of Korea (NRF) Grant funded by the Ministry of Science and ICT (NRF-2022R1A2C1092137).

Data availability The data that support the findings of this study are available within the article.

Declarations

Conflict of interest The authors declare no conflicts of interest.

References

- Abate AR, Weitz DA (2011) Air-bubble-triggered drop formation in microfluidics. *Lab Chip* 11:1713–1716. <https://doi.org/10.1039/c1lc20108e>
- Amoyav B, Benny O (2019) Microfluidic based fabrication and characterization of highly porous polymeric microspheres. *Polymers (basel)* 11:419. <https://doi.org/10.3390/polym11030419>
- Amstad E, Chemama M, Eggersdorfer M, Arriaga LR, Brenner MP, Weitz DA (2016) Robust scalable high throughput production of monodisperse drops. *Lab Chip* 16:4163–4172. <https://doi.org/10.1039/c6lc01075j>
- Bajgiran KR, Cordova AS, Elkhanoufi R (2021) Simultaneous droplet generation with in-series droplet t-junctions induced by gravity-induced flow. *Micromachines* 12:1211. <https://doi.org/10.3390/M12101211>
- Brakke KA (1992) The surface evolver. *Exp Math* 1:141–165. <https://doi.org/10.1080/10586458.1992.10504253>
- Deng C, Wang H, Huang W, Cheng S (2017) Numerical and experimental study of oil-in-water (O/W) droplet formation in a co-flowing capillary device. *Colloids Surfaces A* 533:1–8. <https://doi.org/10.1016/j.colsurfa.2017.05.041>
- Dewandre A, Rivero-Rodriguez J, Vitry Y, Sobac B, Scheid B (2020) Microfluidic droplet generation based on non-embedded co-flow-focusing using 3D printed nozzle. *Sci Rep* 10:21616. <https://doi.org/10.1038/s41598-020-77836-y>
- Du L, Li Y, Wang J, Zhou Z, Lan T, Jing D, Wu W, Zhou J (2023) Cost-effective droplet generator for portable bio-applications. *Micromachines* 14:466. <https://doi.org/10.3390/mi14020466>
- Fu T, Wu Y, Ma Y, Li HZ (2012) Droplet formation and breakup dynamics in microfluidic flow-focusing devices: from dripping to jetting. *Chem Eng Sci* 84:207–217. <https://doi.org/10.1016/j.ces.2012.08.039>
- Glawdel T, Elbuken C, Ren CL (2012) Droplet formation in microfluidic T-junction generators operating in the transitional regime. I. Experimental observations. *Phys Rev E* 85:1–9. <https://doi.org/10.1103/PhysRevE.85.016322>
- Gyimah N, Scheler O, Rang T, Pardy T (2021) Can 3d printing bring droplet microfluidics to every lab? A systematic review. *Micromachines* 12:1–22. <https://doi.org/10.3390/mi12030339>
- Hettiarachchi S, Melroy G, Mudugamuwa A, Sampath P, Premachandra C, Amarasinghe R, Dau V (2021) Design and development of a microfluidic droplet generator with vision sensing for lab-on-a-chip devices. *Sens Actuators A* 332:113047. <https://doi.org/10.1016/j.sna.2021.113047>
- Hoang VT, Lim J, Byon C, Park JM (2018) Three-dimensional simulation of droplet dynamics in planar contraction microchannel. *Chem Eng Sci* 176:59–65. <https://doi.org/10.1016/j.ces.2017.10.020>
- Huang L, Xiao L, Jung Poudel A, Li J, Zhou P, Gauthier M, Liu H, Wu Z, Yang G (2018) Porous chitosan microspheres as microcarriers for 3D cell culture. *Carbohydr Polym* 202:611–620. <https://doi.org/10.1016/j.carbpol.2018.09.021>
- Ibrahim AM, Padovani JI, Howe RT, Anis YH (2021) Modeling of droplet generation in a microfluidic flow-focusing junction for droplet size control. *Micromachines* 12:1–11. <https://doi.org/10.3390/mi12060590>
- Langer K, Bremond N, Boitard L, Baudry J, Bibette J (2018) Micro-pipette-powered droplet based microfluidics. *Biomicrofluidics* 12:044106. <https://doi.org/10.1063/1.5037795>

- Li HT, Wang HF, Wang Y, Pan JZ, Fang Q (2020) A minimalist approach for generating picoliter to nanoliter droplets based on an asymmetrical beveled capillary and its application in digital PCR assay. *Talanta* 217:120997. <https://doi.org/10.1016/j.talanta.2020.120997>
- Montanero JM, Gañán-Calvo AM (2020) Dripping, jetting and tip streaming. *Rep Prog Phys* 83:097001. <https://doi.org/10.1088/1361-6633/aba482>
- Mottaghi S, Nazari M, Fattahi SM, Nazari M, Babamohammadi S (2020) Droplet size prediction in a microfluidic flow focusing device using an adaptive network based fuzzy inference system. *Biomed Microdevice* 22:61. <https://doi.org/10.1007/s10544-020-00513-4>
- Nguyen HV, Nguyen HQ, Nguyen VD, Seo TS (2019) A 3D printed screw-and-nut based droplet generator with facile and precise droplet size controllability. *Sens Actuata B* 296:126676. <https://doi.org/10.1016/j.snb.2019.126676>
- Nie M, Zheng M, Li C, Shen F, Liu M, Luo H, Song X, Lang Y, Pan JZ, Du W (2019) Assembled step emulsification device for multiplex droplet digital polymerase chain reaction. *Anal Chem* 91:1779–1784. <https://doi.org/10.1021/acs.analchem.8b04313>
- Rayleigh L (1878) On the instability of jets. *Proc Lond Math Soc* s1–10:4–13. <https://doi.org/10.1112/plms/s1-10.1.4>
- Rayner M, Trägårdh G, Trägårdh C, Dejmek P (2004) Using the surface evolver to model droplet formation processes in membrane emulsification. *J Colloid Interface Sci* 279:175–185. <https://doi.org/10.1016/j.jcis.2004.06.068>
- Shams Khorrami A, Rezai P (2018) Oscillating dispersed-phase co-flow microfluidic droplet generation: multi-droplet size effect. *Biomicrofluidics* 12:034113. <https://doi.org/10.1063/1.5034473>
- Shang L, Cheng Y, Zhao Y (2017) Emerging droplet microfluidics. *Chem Rev* 117:7964–8040. <https://doi.org/10.1021/acs.chemrev.6b00848>
- Shui L, Mugele F, Van Den Berg A, Eijkel JCT (2008) Geometry-controlled droplet generation in head-on microfluidic devices. *Appl Phys Lett* 93:2006–2009. <https://doi.org/10.1063/1.3000624>
- Takeuchi S, Garstecki P, Weibel DB, Whitesides GM (2005) An axisymmetric flow-focusing microfluidic device. *Adv Mater* 17:1067–1072. <https://doi.org/10.1002/adma.200401738>
- Tan YC, Fisher JS, Lee AI, Cristini V, Lee AP (2004) Design of microfluidic channel geometries for the control of droplet volume, chemical concentration, and sorting. *Lab Chip* 4:292–298. <https://doi.org/10.1039/b403280m>
- Teo AJT, Yan M, Dong J, Xi HD, Fu Y, Tan SH, Nguyen NT (2020) Controllable droplet generation at a microfluidic T-junction using AC electric field. *Microfluid Nanofluid* 24:1–9. <https://doi.org/10.1007/s10404-020-2327-6>
- Trossbach M, de Lucas Sanz M, Seashore-Ludlow B, Joensson HN (2022) A portable, negative-pressure actuated dynamically tunable microfluidic droplet generator. *Micromachines* 13:1823. <https://doi.org/10.3390/mi13111823>
- Umbanhowar PB, Prasad V, Weitz DA (2000) Monodisperse emulsion generation via drop break off in a coflowing stream. *Langmuir* 16:347–351. <https://doi.org/10.1021/la990101e>
- Utada AS, Fernandez-Nieves A, Stone HA, Weitz DA (2007) Dripping to jetting transitions in coflowing liquid streams. *Phys Rev Lett* 99:1–4. <https://doi.org/10.1103/PhysRevLett.99.094502>
- Wang ZL (2015) Speed up bubbling in a tapered co-flow geometry. *Chem Eng J* 263:346–355. <https://doi.org/10.1016/j.cej.2014.11.018>
- Yao J, Lin F, Kim HS, Park J (2019) The effect of oil viscosity on droplet generation rate and droplet size in a T-Junction microfluidic droplet generator. *Micromachines* 10:808. <https://doi.org/10.3390/mi10120808>
- Yin Z, Huang Z, Lin X, Gao X, Bao F (2020) Droplet generation in a flow-focusing microfluidic device with external mechanical vibration. *Micromachines* 11:743. <https://doi.org/10.3390/mi11080743>
- Zhang JM, Ji Q, Duan H (2019) Three-dimensional printed devices in droplet microfluidics. *Micromachines* 10:1–24. <https://doi.org/10.3390/mi10110754>
- Zhang J, Xu W, Xu F, Lu W, Hu L, Zhou J, Zhang C, Jiang Z (2021) Microfluidic droplet formation in co-flow devices fabricated by micro 3D printing. *J Food Eng* 290:110212. <https://doi.org/10.1016/j.jfoodeng.2020.110212>
- Zhou C, Zhu P, Tian Y, Tang X, Shi R, Wang L (2017) Microfluidic generation of aqueous two-phase-system (ATPS) droplets by oil-droplet choppers. *Lab Chip* 17:3310–3317. <https://doi.org/10.1039/c7lc00696a>
- Zhu P, Wang L (2017) Passive and active droplet generation with microfluidics: a review. *Lab Chip* 17:34–75. <https://doi.org/10.1039/C6LC01018K>
- Zhu P, Kong T, Kang Z, Tian X, Wang L (2015) Tip-multi-breaking in capillary microfluidic devices. *Sci Rep* 5:1–8. <https://doi.org/10.1038/srep11102>
- Zhu P, Tang X, Wang L (2016) Droplet generation in co-flow microfluidic channels with vibration. *Microfluid Nanofluid* 20:1–10. <https://doi.org/10.1007/s10404-016-1717-2>

Publisher's Note Springer Nature remains neutral with regard to jurisdictional claims in published maps and institutional affiliations.

Springer Nature or its licensor (e.g. a society or other partner) holds exclusive rights to this article under a publishing agreement with the author(s) or other rightsholder(s); author self-archiving of the accepted manuscript version of this article is solely governed by the terms of such publishing agreement and applicable law.